THE ASTROPHYSICAL JOURNAL, 461:572–586, 1996 April 20

THE DARK MATTER, GAS, AND GALAXY DISTRIBUTIONS IN ABELL 2218: A WEAK GRAVITATIONAL LENSING AND X-RAY ANALYSIS

G. SQUIRES,[1] N. KAISER,[2,3] A. BABUL,[4] G. FAHLMAN,[3,5] D. WOODS,[5]
D. M. NEUMANN,[6] AND H. BÖHRINGER[6]
Received 1995 July 5; accepted 1995 September 22

ABSTRACT

We report on the detection of dark matter in the cluster Abell 2218 using the weak gravitational distortion of background galaxies. We find a highly significant, coherent detection of the distortion in the images of the background galaxies. We use *Hubble Space Telescope* (*HST*) images from the Medium Deep Survey to calibrate the suppression in the observed distortion due to atmospheric smearing. The inferred two-dimensional mass distribution has a peak that is coincident with the optical and X-ray centroid. The qualitative distributions of the cluster light, the X-ray emission, and the dark matter are similar and the projected total mass, gas, and light surface densities are consistent with an r^{-1} profile at a distance of $r > 180''$ from the cluster cD galaxy. Using the weak lensing technique, we determine a lower bound for the total mass in A2218 of $(3.9 \pm 0.7) \times 10^{14}\ h^{-1}\ M_\odot$ within a fiducial aperture of radius 0.4 h^{-1} Mpc. The associated cluster mass-to-light ratio is $(440 \pm 80)\ h\ M_\odot/L_{\odot B}$. The mass estimated by the weak lensing method is consistent with that inferred from the X-ray data under the assumption of hydrostatic equilibrium, and we derive an upper bound for the gas–to–total mass ratio at 400 h^{-1} kpc of $M_{\rm gas}/M_{\rm tot} = (0.04 \pm 0.02)\ h^{-3/2}$. The lensing estimates assumes that a control annulus extending from 0.4–0.7 h^{-1} Mpc is empty. Correcting for the mean surface density matter in the control annulus as inferred from the X-ray data increases the lensing mass estimate by $\simeq 20\%$, and the lensing and X-ray mass estimates are still consistent within the experimental uncertainties.

Subject headings: cosmology: observations — dark matter — galaxies: clusters: individual (A2218) — galaxies: X-rays

1. INTRODUCTION

One of the most compelling problems in astronomy today is understanding the distribution and nature of the ubiquitous dark matter, which dominates the dynamical evolution of much of the observable universe. Historically, much of the strongest evidence for dark matter comes from the virial analysis of clusters of galaxies. The high mass-to-light ratios ($M/L \sim 300\ h$, where the Hubble constant is given by $H_0 = 100\ h$ km s^{-1} Mpc^{-1}) thus obtained are supported by the observed high temperatures of the X-ray–emitting gas and by the presence of giant arcs and arclets in the clusters. The nature and the extent of dark matter distribution in clusters, however, is not well understood. In the past, information regarding the dark matter distribution in clusters could only be extracted from dynamical studies of galaxies or from X-ray surface brightness data, under restrictive assumptions. For example, virial studies generally assume that galaxy orbits are isotropic and that the light traces the dark matter, while analyses of the X-ray data are based on the assumptions that the gas is in hydrostatic equilibrium within the cluster potential and is supported against collapse by thermal pressure. The results of these studies can be in considerable error if these assumptions are not valid. Gravitational lensing, on the other hand, is a well-understood physical process that directly probes the clusters' gravitational potential wells. Hence, studies of both the strong as well as the weak distortions in the images of faint, background galaxies induced by the clusters offer a unique opportunity to directly probe the cluster mass distributions in a model-independent fashion, with the weak distortions being particularly suited for mapping the mass distribution out to large radii.

Mapping the dark matter distribution in clusters using the weak gravitational lensing effect is a subject of great modern interest and is rapidly becoming a mature subject. The procedure was pioneered by Tyson, Valdes, & Wenk (1990), and several groups have discussed techniques for acquiring and analyzing data (Bonnet & Mellier 1995; Kaiser, Squires, & Broadhurst 1995b; Fischer & Tyson 1995). The first fully developed algorithm for constructing cluster mass maps using the weak distortions was proposed by Kaiser & Squires (1993). This algorithm requires shear information extending out to infinity, and applying it to data of finite spatial extent results in a mass map with a small but well-understood bias at the edges of the data region. Minor modifications to the algorithm can correct

---

[1] Physics Department, University of Toronto, 60 St. George Street, Toronto, Ontario, Canada M5S 1A7.

[2] Canadian Institute for Advanced Research and Canadian Institute for Theoretical Astrophysics, University of Toronto, 60 St. George Street, Toronto, Ontario, Canada M5S 1A7.

[3] Visiting Astronomer, Canada-France-Hawaii Telescope, operated by the National Research Council of Canada, le Centre National de la Recherche Scientifique de France, and the University of Hawaii.

[4] Department of Physics, New York University, 4 Washington Place, Room 525, New York, NY 1003-6621.

[5] Department of Geophysics and Astronomy, University of British Columbia, 2219 Main Mall, Vancouver, BC, Canada V6T 1Z4.

[6] Max-Planck-Institut für extraterrestrische Physik, D-85740 Garching bei München, Federal Republic of Germany.

for this bias, and several modified techniques have been proposed (Kaiser & Squires 1995; Schneider & Seitz 1995; Seitz & Schneider 1995a, b). We emphasize that this affects only the two-dimensional reconstructions of the surface density. The aperture densitometry used here and in Fahlman et al. (1994) is entirely free of this bias.

The list of clusters analyzed using these algorithms is growing steadily and includes A1689 (Tyson et al. 1990; Tyson & Fischer 1995; Kaiser et al. 1995a), Cl 1409+52 (Tyson et al. 1990), MS 1224+20 (Fahlman et al. 1994), Cl 0024+17 (Bonnet et al. 1994; Mellier et al. 1994), and Cl 1455+22 and Cl 0016+16 (Smail, Ellis, & Fitchett 1994; Smail et al. 1995). A more complete list appears in the review by Fort & Mellier (1994). All the methods, however, are limited in that the mass surface density can only be determined up to an additive constant. Broadhurst, Taylor, & Peacock (1995) have proposed a method for breaking this baseline degeneracy, and the method was recently applied to A1689 (Kaiser, Broadhurst, & Squires 1995b).

In this paper, we present a study of A2218. A2218 has been studied extensively in several wavelengths. It is an optically compact (Butcher, Wells, & Oemler 1983) Abell richness class 4 cluster (Abell, Corwin, & Olowin 1989) at redshift $z = 0.175$. It has a central velocity dispersion of 1370^{+160}_{-210} km s^{-1} (Le Borgne, Pello, & Sanahuja 1992). A detailed photometric and spectroscopic study of the cluster center suggests that the cluster consists of two galaxy concentrations; the larger of the two is centered about the sole cD galaxy in the cluster, while the smaller concentration is located 67″ to the southeast (Pello-Descayre et al. 1988; Pello et al. 1992). Deep optical images of the cluster have revealed a wealth of arcs and arclets, with the arcs centered about both mass concentrations. The location and the morphology of the arcs suggest that the bulk of the cluster mass is associated with the galaxy concentration surrounding the cD galaxy. Kneib et al. (1995) have attempted to use the arcs to constrain the mass distribution within the central $\sim 130\ h^{-1}$ kpc.

A2218 also exhibits a strong Sunyaev-Zeldovich effect (Birkinshaw, Gull, & Northover 1981; Birkinshaw & Gull 1984; Partridge et al. 1987; Klein et al. 1991; Jones et al. 1993; Birkinshaw & Hughes 1994) and has been well studied in the X-ray. It has an X-ray luminosity of 6.5×10^{44} ergs s^{-1} in the 0.5–4.5 keV band (Perrenod & Henry 1981) and 1×10^{45} ergs s^{-1} in the 2–10 keV band (David et al. 1993). Its *Einstein* IPC image revealed a smooth circular profile (Boynton et al. 1982). The cluster has also been observed using both the *ROSAT* PSPC (Stewart et al. 1994) and HRI instruments. The peak of the X-ray surface brightness distribution is coincident with the location of the cD galaxy, and the temperature of the X-ray–emitting gas has been determined to lie in the range 6–8 keV (McHardy et al. 1990; Yamashita 1995).

In a recent study, Miralda-Escudé & Babul (1995) drew attention to an interesting puzzle concerning A2218: The mass in the central regions inferred from strong lensing distortions is greater than that determined using the X-ray observations by a factor of ~ 2 if the gas is assumed to be in thermal pressure–supported hydrostatic equilibrium. This led them to speculate that perhaps the gas, at least in the central regions, may be partially supported against gravitational collapse by means other than thermal pressure (see also Loeb & Mao 1994). This mass discrepancy, if it extends out to larger radii, has important implications for quantities, such as the cluster gas fraction $M_{\rm gas}/M_{\rm tot}$, derived solely from X-ray data. Typically, the cluster gas fraction is estimated to be $M_{\rm gas}/M_{\rm tot} \sim 0.05\ h^{-3/2}$ (White & Fabian 1995; David, Jones, & Forman 1995), a result that has been a source of much discussion (White 1992; Babul & Katz 1993; White et al. 1993). This value, however, may be an overestimate by as much as a factor of ~ 2 if the X-ray/lensing mass discrepancy discussed by Miralda-Escudé & Babul (1995) extends beyond the cluster core.

In this paper, we use the observed weak distortions in the images of faint background galaxies to determine the surface mass distribution associated with A2218 out to a distance of $\sim 600\ h^{-1}$ kpc. We compare the distribution of total mass to that of the light and the gas (derived from *ROSAT* data). We also compare the lensing estimate of the total projected mass in the cluster with that determined using the X-ray data and estimate the mass-to-light ratio for the cluster as well as the fraction of the total mass contributed by baryons. We compare the latter against constraints from nucleosynthesis. Throughout this paper, we use an Einstein–de Sitter cosmology with $\Omega = 1$, $q_0 = 0.5$, and a Hubble constant parametrized by $H_0 = 100\ h$ km s^{-1} Mpc^{-1}.

2. DATA ACQUISITION

A2218 was observed using the 3.6 m Canada-France-Hawaii telescope on the nights of 1994 June 6–9. The detector used was the 2048 × 2048 Loral 3 CCD at prime focus with a pixel size of 0″.207. Our observing strategy was to take relatively short (20 minute) exposures in each band and observe each field several times, with small random offsets.

Our *I*-band observations of A2218 comprised of seven 20 minute images centered on the cD galaxy, six of which were discarded because of bad seeing conditions, and two 20 minute images of each field in a 2 × 2 overlapping grid about the cluster center. The two exposures of each field were offset by $\sim 10''$. The observations cover an $\simeq 145$ arcmin^2 field, extending to a radius of $\simeq 6'.5$ ($\sim 750\ h^{-1}$ kpc) from the cluster center. The seeing varied from FWHM = 1″.2 during the first night to 0″.7 during the second. We used only the best seeing data in our lensing analysis. Therefore, we have a total of 9 × 20 minute exposures on the cluster (one central field and 2 × 4 grid fields).

We also observed the cluster center in *V*, acquiring two 20 minute exposures with seeing conditions of 1″.0 FWHM. The *V*-band information, in conjunction with the *I*-band data, allowed us to identify the cluster galaxy sequence in the color-magnitude plane in order to facilitate an estimate of the light in the cluster. Also, the total integration of 40 minutes in the *V* band was sufficient to yield an independent mass map out to a radius of 3′.5 ($\sim 400\ h^{-1}$ kpc) from the cluster center.

3. DATA ANALYSIS

The large number of exposures that we collected over the three nights of observing implies that in principle we ought to be able to construct a median sky flat. Unfortunately, all the fields that we observed contain very luminous, extended galaxies. In addition, several stars saturated and contaminated large portions of each exposure. The resulting median sky flat contains "shadows" of these objects. Attempts to mask the luminous galaxies and using only frames with large offsets did not result in any significant improvement. Consequently, we employed the median twilight flat. Dividing each image (after subtracting the bias) with the median twilight flat resulted in an rms noise in the sky background on the individual images of 24.2 mag arcsec^{-1} in I and 25.6 mag arcsec^{-2} in V.

The data were calibrated against photometric standards in the globular clusters M92 and NGC 4147 (unpublished photometry from Davis 1990; see also Stetson & Harris 1988 and Odewahn, Bryja, & Humphreys 1992) and Landolt (1992) standards in SA 110. Color terms were found to be unnecessary in the transformation, and the I and V zero points were determined with a formal error of less than 0.005 mag.

We identified objects on our images, and measured their position and size, using our standard procedure (Kaiser et al. 1995b). Briefly, we smoothed each image with a family of Gaussian filters whose characteristic scales ranged from 0.5 to 100 pixels, varying in logarithmic steps of $d\ln(r) = 0.2$. The upper limit of the range for the filter scale was chosen so that the most luminous and extended galaxies would be comfortably contained within the filter. We tracked the peak trajectories (i.e., the peak significance as a function of smoothing radius) and assigned a radius to each object, r_g, corresponding to the radius of maximum significance (i.e., maximum signal-to-noise). For objects modeled as Gaussian ellipsoids, this radius corresponds to the scale length.

For each object detected, we measured the shape, magnitude, and profile parameters. The magnitude of an object was estimated using an aperture of radius $3r_g$ (i.e., 3 times the radius of maximum significance). The weighted quadrupole moments, Q_{ij}, of the surface brightness distribution were determined using a bi-linear model for the local sky determined in a 16–32 pixel collar around each peak. The analysis employs a Gaussian weighting function whose scale is matched to the object's radius of maximum significance. For Gaussian objects, this choice is optimal.

The perturbation to the observed surface brightness due to a planar lens is $f'(\theta_i) = f(\theta_i - \phi_{,ij}\theta_j)$, where ϕ is the surface potential satisfying Poisson's equation $\nabla^2\phi = 2\Sigma/\Sigma_c = 2\kappa$, and $\phi_{,ij} \equiv \partial^2\phi/\partial x_i \partial x_j$. Here $\Sigma_{\rm crit}^{-1} = 4\pi G D_l \beta$ is the critical surface density, D_l is the angular diameter distance to the lens, and $\beta = \max\,(0, \langle 1 - w_l/w_s \rangle)$. In an Einstein–de Sitter universe with $\Omega = 1$, the comoving distance w is defined as $w = 1 - 1/(1+z)^{1/2}$. In the weak lensing limit, the effect of a planar lens can be represented as a perturbation to the intrinsic quadrupole moment of an object's surface light distribution.

We used the measured quadrupole moments to form a two-component polarization

$$\epsilon_1 = \frac{Q_{11} - Q_{22}}{Q_{11} + Q_{22}} \quad \text{and} \quad \epsilon_2 = \frac{2Q_{12}}{Q_{11} + Q_{22}} . \tag{3.1}$$

Assuming that the $\phi_{,ij}$ terms are small and constant over the size of the galaxy image, we can relate the two polarization components (ϵ_1, ϵ_2) to the derivatives of the potential. For unit weighting and intrinsically circular objects, the polarization is related to the shear, γ, as $\epsilon_\alpha = 2\gamma_\alpha$, where $\gamma_1 = (\phi_{,11} - \phi_{,22})/2$ and $\gamma_2 = \phi_{,12}$.

For non–unit weighting (which is necessary to suppress divergent sky noise contributions), the first-order shift in polarization induced by the shear is (Kaiser et al. 1995b)

$$\delta\epsilon_\alpha = P_{\alpha\beta}^{\rm shear}\gamma_\beta , \tag{3.2}$$

where $P_{\alpha\beta}^{\rm shear}$ defines the shear polarizability tensor. This tensor can be expressed as a combination of the angular moments of the surface brightness, the weight function, and its derivatives. Consequently, it can be computed using quantities measured directly from each galaxy image. The details of the calculation are involved and are described in Kaiser et al. (1995b). Here we simply wish to highlight that the observed polarization is related to the shear (and hence the lens surface potential) in a simple linear manner.

Gravitational lensing is not the only process that can introduce perturbations in an image's quadrupole moment. Various other effects, such as guiding errors, wind shake, etc., can cause similar distortions. Fortunately, these can be measured. In the absence of these nongravitational effects, the images of the stars in the field would be circular. The smearing due to these effects introduces an anisotropy in their point-spread function (PSF). We model these nongravitational distortions as a convolution of the actual light distribution of individual images with a small but highly anisotropic kernel $g\theta$. The calculation of the effect in the images is very similar to the above and the resulting shift in the polarization depends only on angular moments of $g(\theta)$. Specifically,

$$\delta\epsilon_\alpha = P_{\alpha\beta}^{\rm smear} p_\beta , \tag{3.3}$$

where $p_1 = q_{11} - q_{22}$ and $p_2 = 2q_{12}$ (Kaiser et al. 1995b). To first order in p_α,

$$q_{ij} = \int d^2\theta\,\theta_i\theta_j g(\theta) . \tag{3.4}$$

The smear polarizability tensor $P_{\alpha\beta}^{\rm smear}$ again depends only on the observed object surface brightness, the weight function, and its derivatives.

The anisotropy in the PSF (characterized by p_α) can be determined and corrected for as follows: We isolate the stars based on a size-magnitude cut, and for each stellar image, we measure the polarization ϵ_α, which in effect is a measure of the perturbation since the actual images are expected to be circular. Since the smear polarizability tensor for intrinsically circular objects is diagonal and its elements can be determined from measured quantities, we can compute $p_\alpha = \epsilon_\alpha / P_{\alpha\alpha}^{\rm smear}$ directly (no summation) as a function of position across the frame. Each object's polarization is then corrected by $-P_{\alpha\beta}^{\rm smear} p_\beta$, which restores the polarization to what would have been observed had the PSF been perfectly isotropic.

4. PHOTOMETRY

In Figure 1, we plot the half-light radius $r_{\rm hl}$ versus magnitude of all objects detected in the I-band data, and in Figure 2, we do the same for the V-band data. The points enclosed within the rectangles define the stellar loci. In constructing the catalogs, we masked the regions in the neighborhood of very bright stars as well as in the corners of the fields (these were affected by vignetting), and we selected objects on each frame independently, requiring a significance of $\nu > 4\ \sigma$ over the local sky background. The significance threshold was determined after some experimentation with *HST*

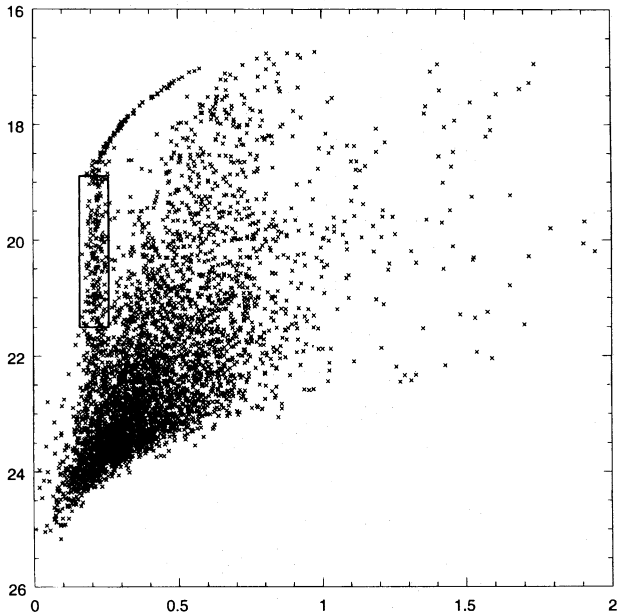

FIG. 1.—The half-light radius vs. I magnitude for all objects in our field. We detect 4444 objects with significance $\nu > 4\ \sigma$ over the local sky background for a surface density of $\bar{n}_I \simeq 30$ per square arcminute. The rectangle delineates the stellar locus.

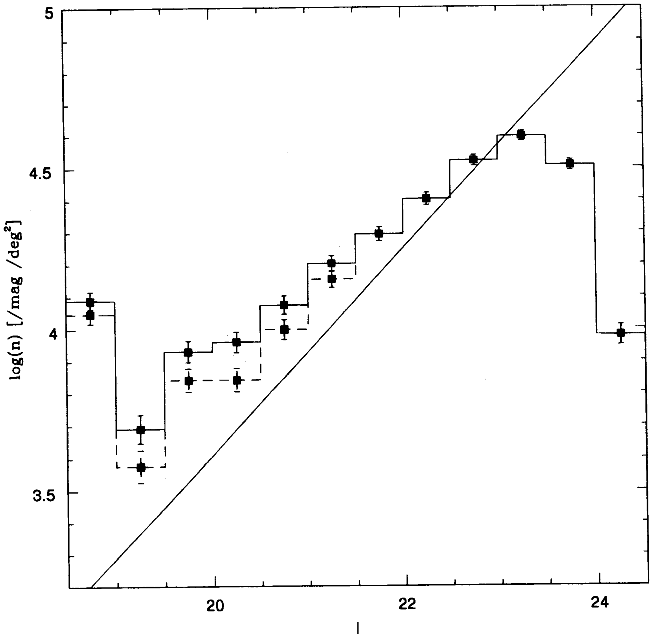

FIG. 3.—The counts per square degree per magnitude from the I-band data. The solid histogram is using all objects; the dashed histogram comes from removing bright stars ($I < 21.5$). The solid line is a fit to the Woods et al. (1995) counts. At the brighter magnitudes, we see an excess in the counts due to the cluster galaxies. At $I \simeq 22$, the counts agree reasonably well with the field counts. The sample is complete to $I \simeq 23$.

images. We found that this procedure, rather than a magnitude selection, was preferable, as it resulted in a higher signal-to-noise ratio when measuring the shear. We only retained objects that are detected on at least two of our nine exposures within a tolerance of 2 pixel positional coincidence. We used the same selection criteria to identify objects in our V-band data. In all, we detected 4444 objects in the I band and 1355 in the V, corresponding to a surface density (of galaxies and stars) of $\bar{n}_I \simeq 30$ arcmin^{-2} and $\bar{n}_V \simeq 28$ arcmin^{-2}, respectively.

We used our catalogs to construct the I- and V-band number-magnitude counts. In Figures 3 and 4, we compare these counts to the I-band counts of Lilly (1993) and the I- and V-band counts of Woods, Fahlman, & Richer (1995). We computed the counts using all the objects (*solid histogram*) and after eliminating all objects that lie on the

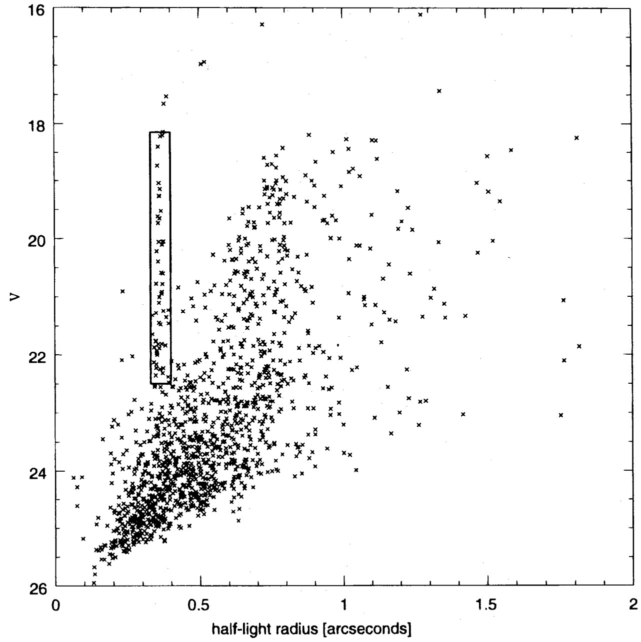

FIG. 2.—The half-light radius vs. V magnitude for all objects in our field. We detect 1355 objects with significance $\nu > 4\ \sigma$ over the local sky background for a surface density of $\bar{n}_V \simeq 28$ per square arcminute. The rectangle delineates the stellar locus.

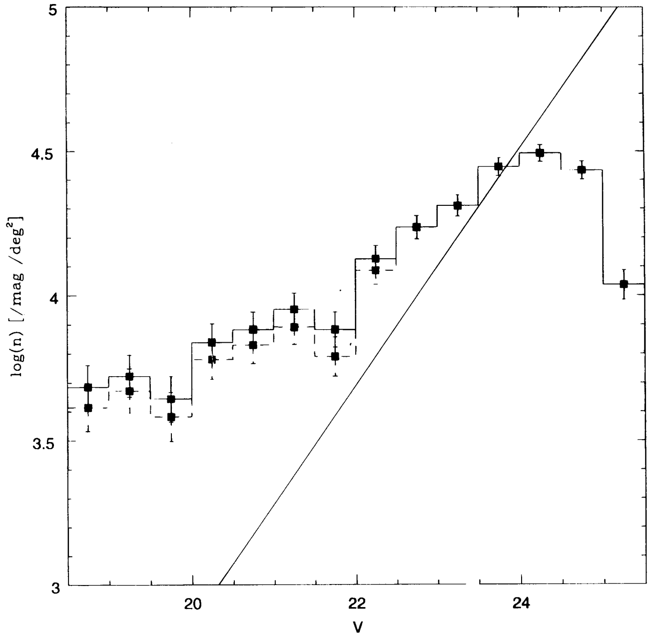

FIG. 4.—The counts per square degree per magnitude from the V-band data. The solid histogram is using all objects; the dashed histogram comes from removing bright stars ($V < 22.5$). The solid line is a fit to the Woods et al. (1995) field counts.

1996ApJ...461..572S

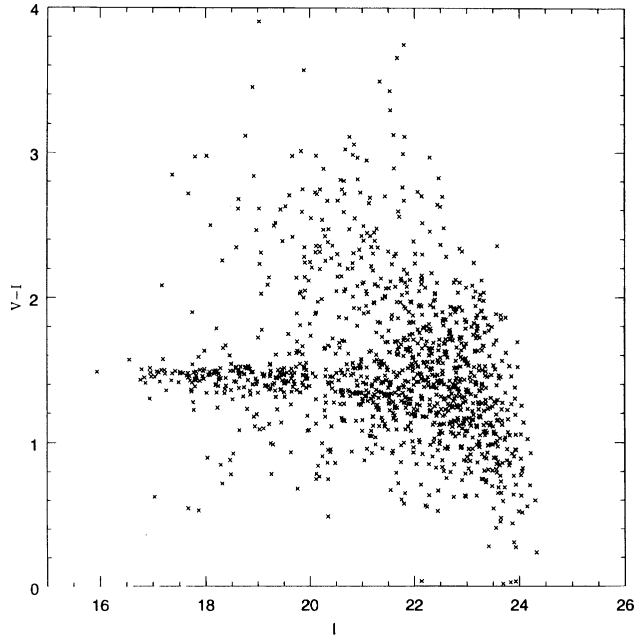

FIG. 5.—The $V-I$ color vs. I for the center field

stellar locus in Figures 1 and 2 (*dashed histogram*). The counts are complete to $I \simeq 23$ and $V \simeq 24$. As the plots show, the counts in our frames are elevated with respect to the field counts, particularly at bright magnitudes. Removing the stars does not eliminate this discrepancy. The excess is mainly due to contamination by cluster galaxies, which we have not attempted to remove. The agreement with the field counts improves toward fainter magnitudes.

In Figure 5, we display the color-magnitude diagram for the central field. A red sequence of objects with a mean color of $V - I \simeq 1.6$ at the bright end is clearly distinguishable. We identified these objects as cluster galaxies. To extract this sample, we fitted a linear model to the color sequence and selected objects with color within 0.2 mag of the mean. In Figure 6, we plot the I-band number counts for the color-selected sample of cluster galaxies. The sample contains 196 galaxies with $I < 20.25$. The number of objects per magnitude is roughly constant. Fitting the cluster luminosity function with a Schecter function $n(m) = A10^{-0.4m(\alpha+1)}$ yields $\alpha = -1$ for the faint end slope.

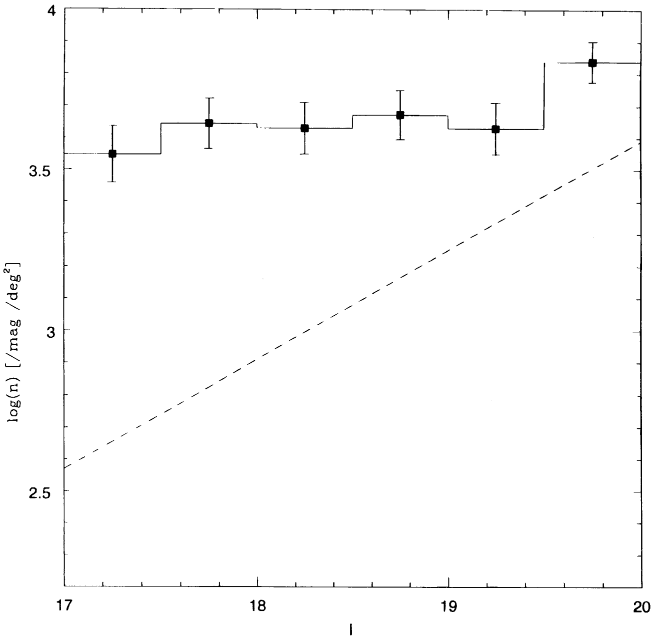

FIG. 6.—The counts per square degree per I magnitude for objects with $I < 20.25$ and color within ± 0.2 mag of a linear fit to the color sequence. The dashed line shows the Woods et al. (1995) field counts.

5. LIGHT DISTRIBUTION

We computed the galaxy surface number density distribution as well as the corresponding light distribution using all the galaxies in the images. To reject obvious foreground galaxies, we applied a very conservative mask. We removed the bright spiral galaxy to the northeast of the cD galaxy but allowed its companion to remain. The giant elliptical to the east is very likely to be a foreground object as well. We allowed it to remain in the calculation of the light distribution, however, as there is a significant overdensity of galaxies in its vicinity, suggesting that there is perhaps a group or small cluster associated with the galaxy.

We display the light and galaxy surface number density as contour plots superposed on the optical image of the cluster in Figures 7 and 8, respectively. The contours have been smoothed with a Gaussian smoothing scale of 0'.67 and are broadly similar. The peak of the light map (Fig. 8) is centered on the primary galaxy clump (the one containing the cD galaxy) in the cluster, and the surface brightness drops off smoothly toward the cluster periphery. In the central region, the contours are elliptical, with the major axis aligned with the primary and secondary galaxy concentrations as well as the chain of bright galaxies stretching away from the cD galaxy in the northwest direction. At distances greater than ~2' from the cD galaxy, the contours show a weak extension toward a giant elliptical galaxy to the east of the cD galaxy. The surface number density plot (Fig. 7) has a very similar morphology. The peak and orientation of ellipticity matches that of the light map. The extension to the east is more evident and extends beyond the giant elliptical galaxy. In addition, there are extensions roughly to the north, south, and west/northwest. Employing the color-selected bright galaxy sample in place of the entire galaxy sample yields a very similar galaxy number density and light distribution. The peak and central ellipticity match that of the entire galaxy population in the images. There is some weak evidence of the extension toward the east, but it is not well resolved in the color-selected sample.

While qualitative descriptions of the light and galaxy distributions are useful, to understand the nature of the distributions and to make comparisons with the distributions of gas and total mass in the cluster, we need to be more quantitative. The usual approach is to compute the mass-to-light ratio as a function of radius. In principle, we can use the excess in the number of galaxies over the field counts to estimate the number of galaxies in the cluster and, hence, to estimate the cluster light; however, we prefer a more simple approach. We make two measurements, which place upper and lower bounds on the cluster light.

To determine the upper bound, we estimate the light contributed from *all* galaxies in our observations. This sample will certainly contain many field galaxies and hence it yields

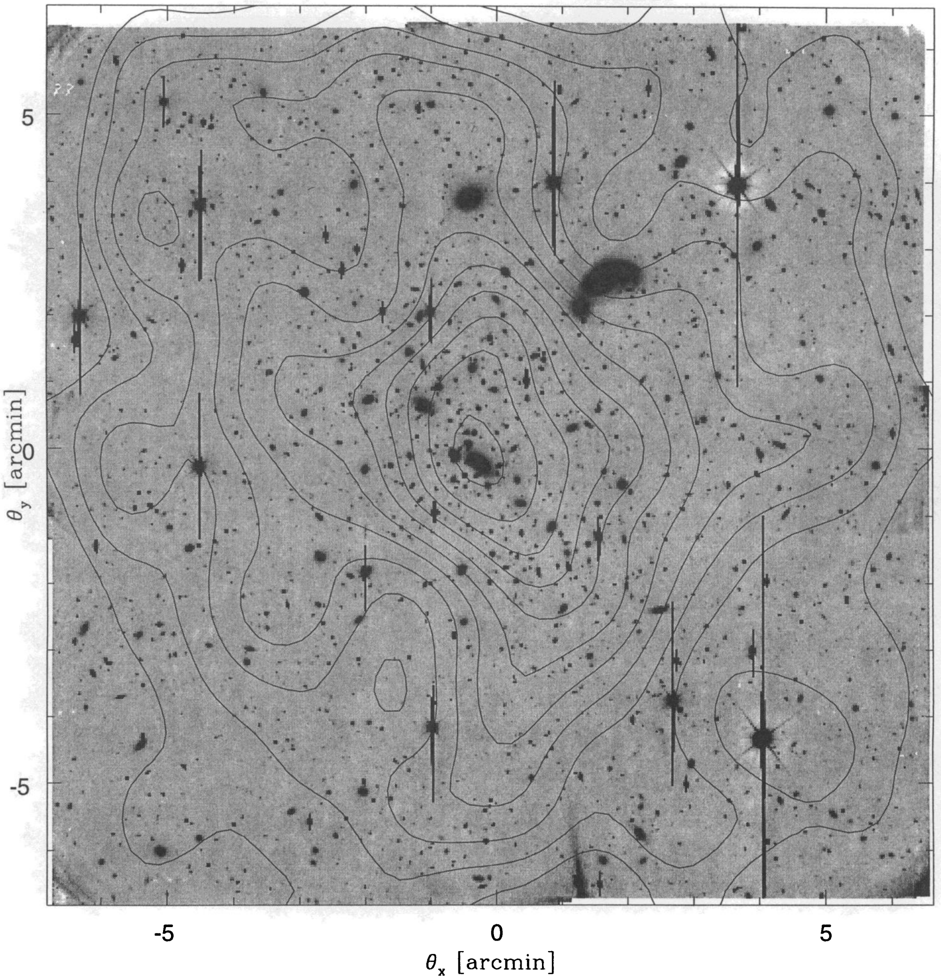

FIG. 7.—The smoothed surface number density of galaxies (*contours*) placed on the optical I-band image of the cluster center. The contours have been smoothed with a Gaussian of scale length 0′.67. North is to the right; east is up.

an overestimate of the light contributed by the cluster galaxies. We work directly with the co-added V image and compute a cumulative, circularly averaged, radial light profile centered on the cD galaxy. We select all objects that were detected on both the V-band images and identify as galaxies all objects having half-light radius greater than 1.2 times the mean stellar half-light radius. We mask all the galaxies on the image and determine a light profile of the resulting image. The light profile of the galaxies is then determined by subtracting the profile of the masked image from that of the unmasked image.

To establish the lower bound, we do a similar analysis using only our bright color-selected galaxy sample. At the bright end, we do not expect much contamination from the field galaxies; most galaxies ought to be cluster members. The color-selected sample, however, excludes all faint ($I > 20.25$) cluster galaxies as well as bright cluster galaxies that lie outside the color sequence. Hence, the resulting cumulative light profile corresponds to a lower bound on the total cluster light.

The two cumulative light profiles described above are shown in Figure 9. The solid line corresponds to the light profile computed using all the galaxies, and the short-dashed line corresponds to that computed using only the bright, red cluster galaxies. At a fiducial radius of 3′.5 (~ 400 h^{-1} kpc), the total apparent magnitude is $V = 13.68$, while that computed using only the red galaxies is $V = 13.96$. These two estimates place an upper and lower bound on the cumulative magnitude at this radius. We determine also the cumulative V-band profile using all galaxies in the more spatially extended I-band images, converting from I to V by applying a color transformation of $V - I = 1.6$, which matches the bright end of the color sequence. In the region in which the two profiles overlap, the latter profile (the long-dashed line in Fig. 9) agrees very well with that computed directly using the V-band data.

It is customary to quote the luminosity (or the luminosity profile) in the B band. We estimate the B-band luminosity for A2218 using our apparent V magnitudes as

$$L_B = 10^{0.4[M_{B\odot} - V - (B-V) + DM + K]} \, L_\odot \, , \quad (5.1)$$

where $M_{B\odot} = 5.48$ is the total solar B magnitude. We apply a K-correction of $K = 0.3$ and a color transformation of $B - V = 0.93$, as suggested by the data in Coleman, Wu, & Weedman (1980). Since A2218 is at redshift $z = 0.175$, its distance modulus is $DM = 38.69$ (for $\Omega = 1$ and $h = 1$).

The cumulative B-band luminosity, as a function of radius, is plotted in Figure 10. Within the central $\sim 100''$, the profile agrees reasonably well with that of Kneib et al. (1995). At larger radii, the cumulative light in the cluster increases linearly with r, suggesting that the optical surface brightness varies with radius as $1/r$. At a fiducial radius of

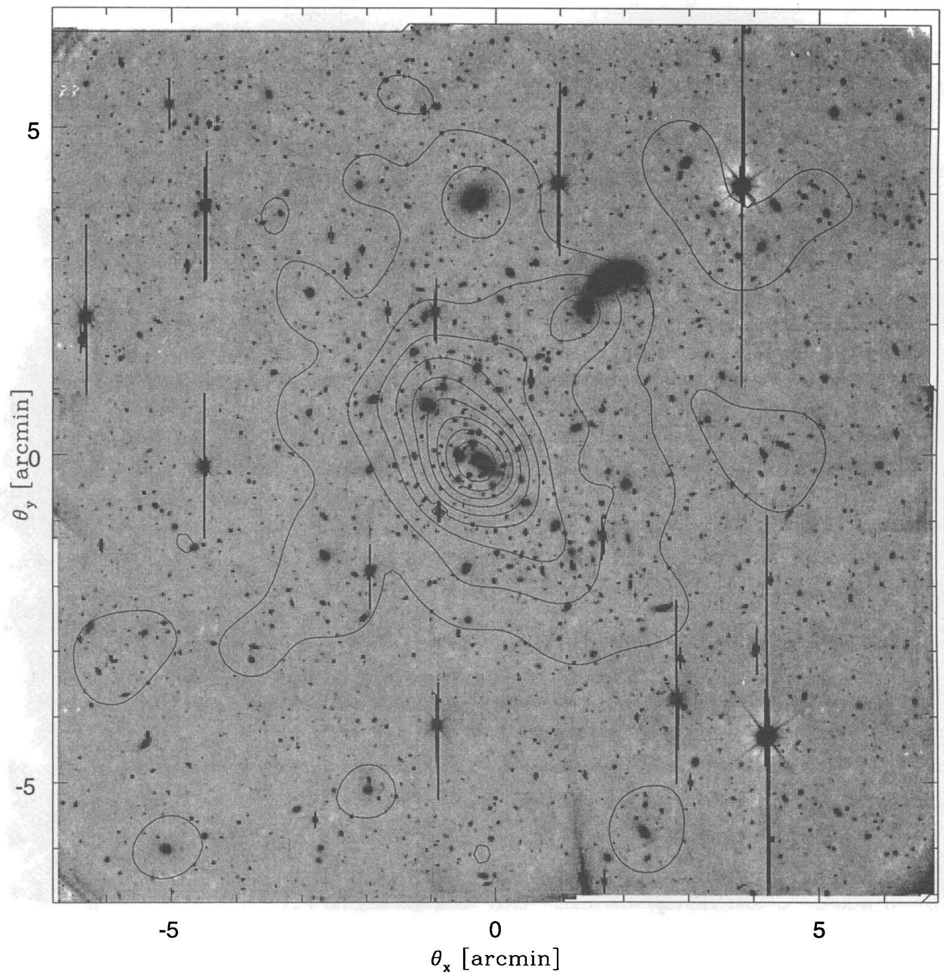

FIG. 8.—The smoothed light from all the galaxies (*contour*) superimposed on the optical image of the cluster field. The light contours have been smoothed with a Gaussian of scale length 0'.67. North is to the right; east is up.

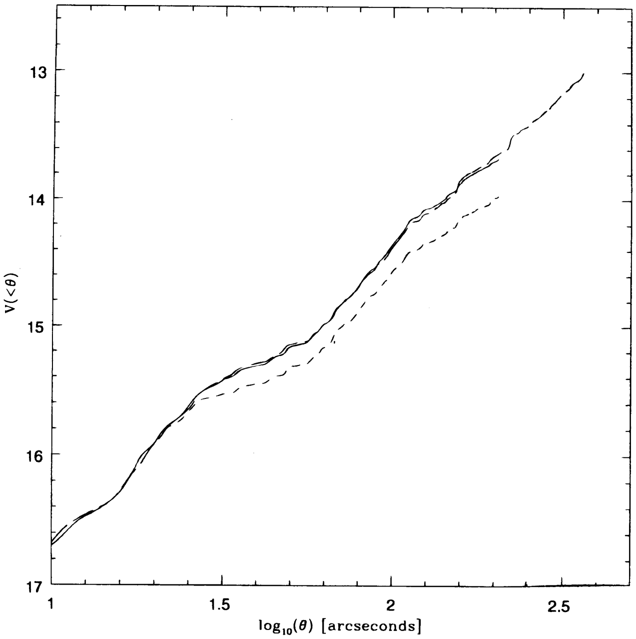

FIG. 9.—The cumulative V magnitude as a function of radius from the cD galaxy. The solid line comes from the V-image; the short-dashed line is the red cluster galaxy contribution to the light. The long-dashed line is the calculation done on the I-band image with a transformation to V being done with a constant color shift of $V-I=1.6$.

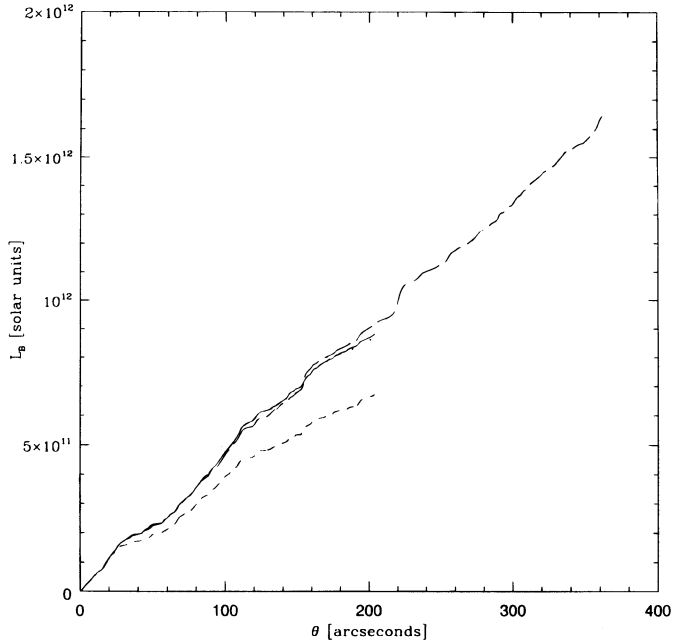

FIG. 10.—The cumulative luminosity as a function of radius from the cD galaxy. The lines are as described on Fig. 9.

$3\rlap{.}'5$ ($\sim 400\ h^{-1}$ kpc), the estimated B-band luminosity of the cluster is in the range 6.8–8.8 $\times\ 10^{11}\ h^{-2}\ L_{\odot}$.

6. LENSING ANALYSIS

As discussed in § 3, we used the stellar PSF to determine and correct for the distortions introduced by nongravitational influences in the images of all objects on a given frame (see eqs. [3] and [4]). We found that the spatial variations in the PSF, over a given image frame, is well modeled by a second-order polynomial. The constant term in the polynomial is benign for our lensing analysis: a uniform shear does not affect our reconstructions of the surface mass density. However, the gradient and the higher order terms are important, and contaminations affecting these quantities are more worrisome. In the uncorrected images, we found a gradient in the stellar PSF that corresponded to a shift in polarization of 4% across each frame. In the cluster outskirts, this is approximately equal to the signal we are trying to measure, and so it clearly must be removed. In addition, we found that the distortions in the stellar PSF, particularly the values of the second-order terms in that expansion, varied from frame to frame. This is not too surprising and is likely due to the unintended rotation of the bonette between exposures. These second-order terms, however, introduce only a small correction, and their inclusion in the analysis resulted in only a very slight improvement over the gradient model, as measured by the change in the residual χ^2 value.

We show the PSF for one of our frames in Figure 11. The raw frame (*left panel*) has a mean $\epsilon_1 = -0.07$. The right panel shows the polarization after the correction is applied. In this case, we are left with a residual mean polarization of 0.0008. In all our corrected frames, the residual polarization is ≤ 0.005.

As discussed previously, we identified as galaxy candidates those objects, on each corrected frame, that appear on at least two frames and have a half-light radius at least 1.2 times larger than the stellar PSF ($r_{\rm hl} > 0\rlap{.}''26$). We then designated those galaxies with magnitudes $I > 21$ as background objects. This yielded a catalog containing 2370 background galaxies over an area of 145 arcmin^2 around the cluster center. We converted the individual polarization estimates to shear measurements according to equation (3.2).

Next, we calibrated the effect of atmospheric seeing, which tends to diminish the shear. We used the Medium Deep Survey (MDS) data from the *Hubble Space Telescope* to accomplish this. The raw *HST* images have roughly twice the resolution of our CFHT data and are unaffected by the atmosphere. The combination of the two data sets allowed us to quantify the damping of the shear due to atmospheric smearing. Using the WFPC2 fields, we constructed a mosaic that is twice the size of our survey field and applied a constant shear of amplitude $\gamma = 0.15$. The latter simulates well the effect of lensing on the galaxy population by a low-redshift cluster. We then rebinned the pixel size to match the resolution of our CFHT data and applied a Gaussian smoothing to simulate the observed seeing conditions. Strictly, this should slightly underestimate the dilution of the measured shear due to seeing, since the observed PSF has a small extended wing compared with a Gaussian. However, since we compute centrally weighted quadrupole moments, the slight extension of the PSF contributes a minimal amount, and the results presented here do not change if we use the shape of the PSF measured from our data. Finally, we added sky noise comparable to that in our observations. The resulting image was processed in exactly the same manner as the real data. Since we are using real galaxy images as input and are simulating, as nearly as possible, the observing conditions we had for our program, we are able to calibrate empirically the loss in the shear signal. In this fashion, we also do not need to model the intrinsic distributions of galaxy sizes, magnitudes, and ellipticities.

Subjecting the simulated CFHT images to the same significance, size, and magnitude cuts as the data, we found that for the I-band data we were able to recover 50% ± 3% of the input signal, with the dispersion being estimated from the scatter over several simulations. All our shear estimates are boosted by this factor. In Figure 12, we display the mean shear calculated on a 16 × 16 grid placed on the I-band image of the field about A2218. The grid calculation ensures that all points are strictly independent. The visual pattern is suggestive, and the tangential alignment around the cD galaxy is evident.

In the upper panel of Figure 13, we plot the mean radial tangential shear profile, using the cD galaxy as the center. The upper dashed line shows the prediction for a singular isothermal sphere with the observed velocity dispersion of 1370 km s^{-1} (Le Borgne et al. 1992) , while the lower line corresponds to $\sigma = 1000$ km s^{-1}. In the lower panel, we display the statistic (Kaiser et al. 1995a)

$$\begin{aligned}\zeta(\theta_1, \theta_2) &= 2(1 - \theta_1^2/\theta_2^2)^{-1} \int_{\theta_1}^{\theta_2} d\ln(\theta)\langle\gamma_t\rangle \\ &= \bar{\kappa}(\theta_1) - \bar{\kappa}(\theta_1 < \theta < \theta_2)\,, \qquad (6.1)\end{aligned}$$

which measures the mean surface density interior to θ_1 relative to the mean in an annulus $\theta_1 < \theta < \theta_2$. The dashed lines show the predictions for the two isothermal sphere models assuming that the cluster extends into the control annulus.

We repeated this analysis for our V-band data and display the corresponding radially averaged tangential shear profile and the ζ statistic in Figure 14. The similarity between the V- and I-band results is reassuring; the fact that the measured shear estimates are reproducible in different wavelengths implies that we are not introducing some wavelength-dependent bias in our analysis.

The plots in Figures 13 and 14 show that for $r > 180''$ ($r > 340\ h^{-1}$ kpc), the measured tangential shear is consistent with that expected from a singular isothermal mass distribution with the observed velocity dispersion ($\sigma = 1370$ km s^{-1}). Interior to this, the measured shear more closely corresponds to that expected from a $\sigma = 1000$ km s^{-1} isothermal mass distribution. One can interpret this trend as implying that the velocity dispersion characterizing the mass distribution in the cluster is $\sigma \sim 1000$ km s^{-1} out to a radius of $r = 100''$ ($r = 190\ h^{-1}$ kpc) from the cD galaxy and then increases smoothly to $\sigma \sim 1370$ km s^{-1} at larger radii. Alternatively, the cluster velocity dispersion may very well be constant throughout the cluster, but the observed value of shear in the central region is suppressed because the sample of galaxies used to compute the shear is strongly contaminated with cluster galaxies. Certainly, we can get an indication that shear suppression due to cluster contamination is indeed happening by focusing only on those galaxies with colors redder than the main cluster sequence. By and large, these galaxies will be background objects. The resulting mean tangential shear at small radii is greater than

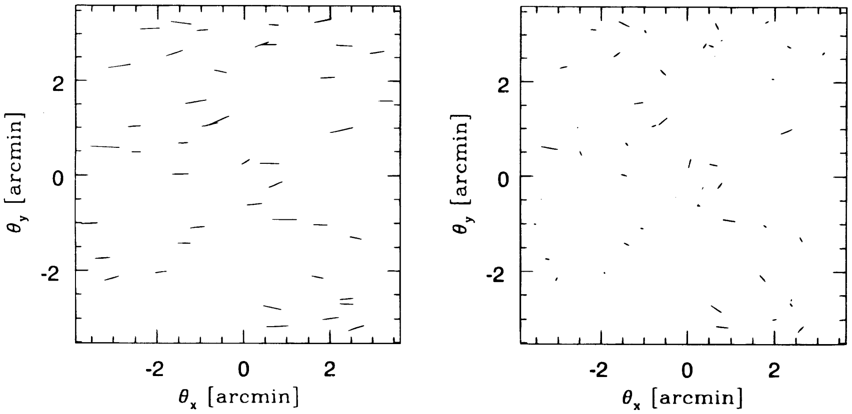

FIG. 11.—The point-spread function for one of the *I*-band images. *Left*: the major axis of objects identified as stars in the field. *Right*: the major axis of the stars after the correction has been applied. We use a frame-dependent, second-order model for the PSF. Here the raw frame had a net $\epsilon_1 = -0.07$, while after the correction is applied the residual $\epsilon_1 = 0.0008$. The residual polarization was $<0.5\%$ for all our corrected frames.

that determined using all galaxies. Unfortunately, the number of red background galaxies is small and hence, we are unable to offer anything more definitive. In any case, our conversion of the measured quadrupole moments of the galaxy image into shear is based on the assumption that the derivatives $\phi_{,ij}$ of the surface potential are small. This assumption certainly breaks down in the central regions of the cluster.

At large radii, the cluster contamination is not an important consideration. Each of the points in Figure 13 with $r > 180''$ corresponds to an average over ≥ 300 galaxies. Furthermore, the measured shear is small (of the order of 10%) and hence, we are confident about the results yielded by our analysis.

Turning back to the actual distribution (as opposed to the radial profile) of shear across cluster, we used the maximum probability extension of the original inversion algorithm (Kaiser & Squires 1993, 1995) to construct a map of the dimensionless surface (total) mass density, κ. This modified algorithm takes into account the finite nature of

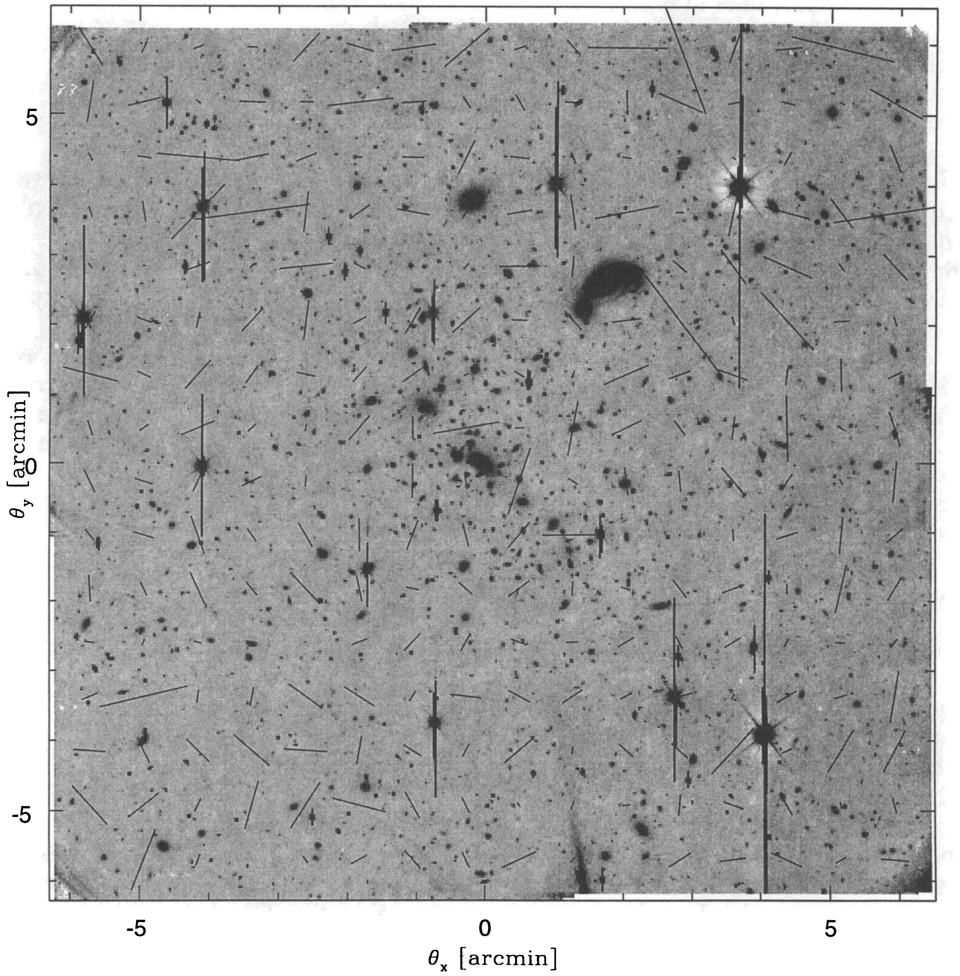

FIG. 12.—The mean shear calculated on a 16 × 16 grid placed on the *I*-band image of the field. The length of the vector is proportional to the shear, with the longest line being equivalent to a shear of 65%.

1996ApJ...461..572S

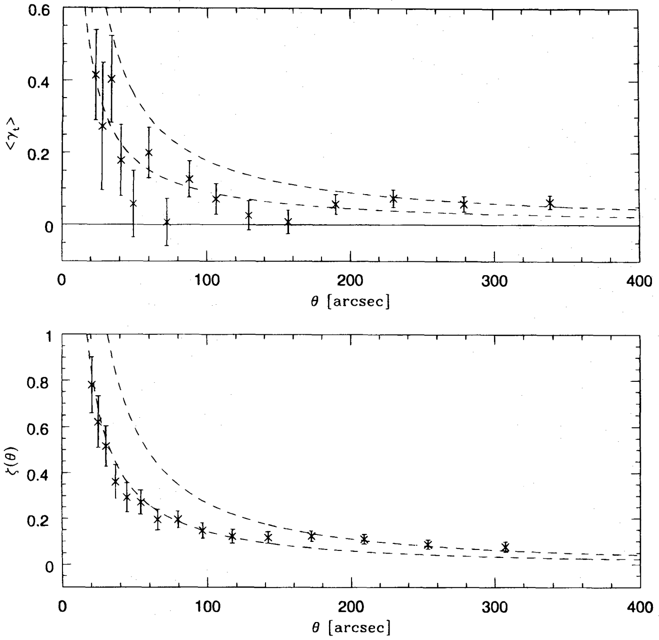

FIG. 13.—The radially averaged tangential shear from the I-band data. The dashed line are predictions of the isothermal sphere model with $\sigma = 1000$, 1370 km s^{-1}, respectively. The bottom panel shows the statistic which measures the mean κ interior to θ, relative to the mean κ in the annulus $\theta < \theta' < 373''$. The error bars are estimated from the orthogonal shear component ; this will overestimate the error if the shear pattern is noncircular.

the data and yields an unbiased estimator of the surface mass density with very low noise properties. In Figure 15, we superpose the contour map of the reconstructed κ on the optical image of the cluster. The contour maps have been smoothed with a Gaussian of scale length 0.′67. The location of the dominant peak coincides with the position of the cluster cD galaxy with a secondary peak approximately 3′ away toward the east. There is, however, no resolved peak associated with the secondary galaxy concentration, although the isodensity contours in the vicinity of the cD galaxy are elongated toward the secondary concentration. Away from the cD, the isodensity contours show extensions toward the north, west, east and south-by-southeast, with the eastern extension forming a bridge between the two peaks.

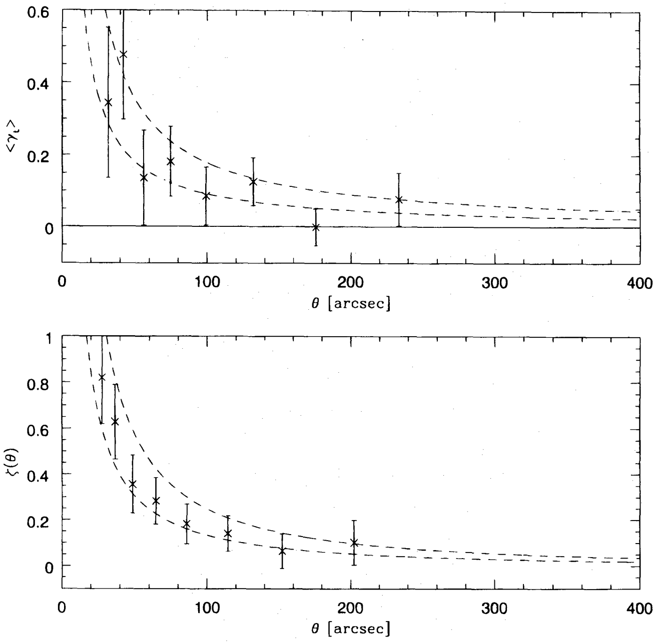

FIG. 14.—The radially averaged tangential shear from the V-band data. The solid lines are the isothermal sphere models with $\sigma = 1000$, 1370 km s^{-1}. The errors are calculated from the second moment of the orthogonal shear component.

In order to convert κ, the dimensionless surface density, into a physical quantity, we need to determine the critical surface density $\Sigma_{\rm crit} = (4\pi G D_l \beta)^{-1}$. For low-redshift clusters, the value of $\Sigma_{\rm crit}$ is only weakly dependent on the background galaxy redshift distribution (Kaiser et al. 1995b). We adopted a value of $\beta = 0.6$ as suggested by an extrapolation of the observed redshift distribution (Lilly 1993, 1995; Tresse et al. 1993) to fainter magnitudes and hence, $\Sigma_{\rm crit} = (7.0 \pm 0.7) \times 10^{15}\ h\ M_\odot$ Mpc^{-2}, where we assumed a 10% uncertainty in β. We note that the value of β is not very sensitive to the model used to estimate the redshift distribution; for example, the model for the faint galaxies of Gronwall & Koo (1994) yields $\beta = 0.59$.

In Figure 16, we plot the two-dimensional mass profile of the cluster. The solid line is the mass profile of a singular isothermal model with a velocity dispersion of 1370 km s^{-1} and whose mass profile extends into the control annulus. We also plot the projected mass at $r = 21''$ (40 h^{-1} kpc), the presumed critical radius determined from one of the giant arcs with redshift $z = 0.7$ (see Miralda-Escudé & Babul 1995), as well as the projected mass at $r = 68''$ (130 h^{-1} kpc) implied by the mass model proposed by Kneib et al. (1995) in order to account for the positions and the morphologies of the giant arcs. The mass estimate of Kneib et al. (1995) is in reasonable agreement with the $\sigma = 1370$ km s^{-1} isothermal prediction at a radius of $\simeq 1'$—their mass estimate actually corresponds to a singular isothermal with a velocity dispersion of $\sigma = 1200$ km s^{-1}—but is higher than the weak lensing result. This is not surprising, since the weak lensing mass estimates at small radii are expected to underestimate the true mass, as we have already discussed. At radii at which we have confidence in the weak lensing results ($r > 180''$), the projected mass profile is consistent with that of the $\sigma = 1370$ km s^{-1} isothermal model (i.e., $\Sigma_{\rm tot} \sim 1/r$), although there is a slight indication that the mass profile might be slightly steeper.

7. X-RAY ANALYSIS

Abell 2218 was observed by *ROSAT* both with the PSPC (position sensitive proportional counter) on 1991 May 25–26 for 44,530 s and with the HRI (high resolution imager) on 1994 January 5–7 and 1994 June 17–19 for a total 35,809 s. The X-ray emission originates from the hot intracluster medium (ICM) contained within the gravitational potential of the cluster. A contour plot of the HRI X-ray surface brightness, superposed on the optical image of the cluster, is presented in Figure 17. The X-ray map has been smoothed with a Gaussian filter of scale 0.′23. The X-ray contours are elliptical, and the position angle of the major axis varies with distance from the central peak. This peak is coincident with the cD galaxy, and there is no evidence of enhanced emission (a secondary peak) associated with the second of the two galaxy concentrations (see also Kneib et al. 1995) although at distances of 1.′5–2′ from the central peak, the X-ray contours show extensions in the southeast (encompassing the secondary mass concentration), north, and west/west-by-northwest directions.

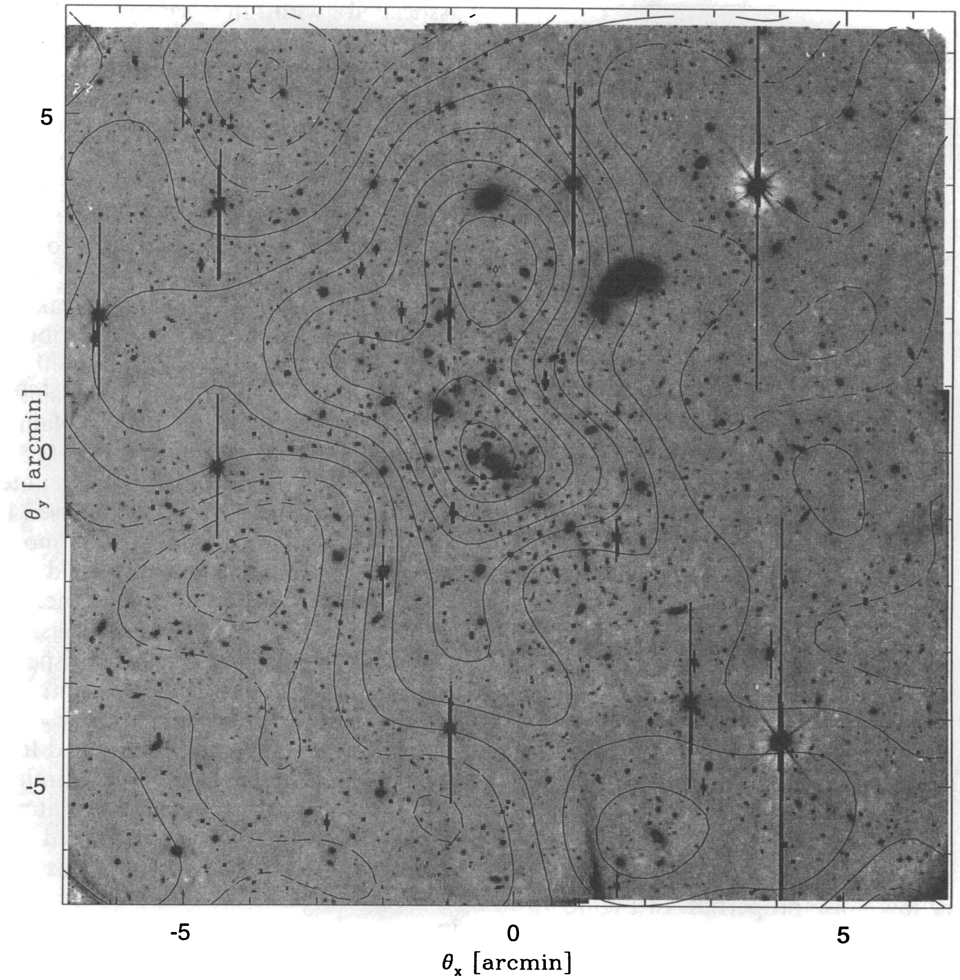

FIG. 15.—The reconstructed surface density using the maximum probability extension to the original Kaiser-Squires algorithm. The contours have been smoothed with a Gaussian with scale length 0'.67.

The radial profile of the observed X-ray surface brightness of A2218 (see Fig. 2 of Miralda-Escudé & Babul 1995) can be well fit by a function of the form

$$S(r) = S_0\left(1 + \frac{r^2}{r_c^2}\right)^{-3\beta+1/2} , \qquad (7.1)$$

where S_0 is the central surface brightness and r_c is the core radius (e.g., Fabricant & Gorenstein 1983). To minimize contamination by the background, we only used the PSPC data in the 0.5–2 keV band and fitted the radial profiles for each of the four quadrants separately. The resulting values of r_c and β are presented in Table 1. To account for the possible smoothing of the X-ray data by the PSF of the detector, we applied Lucy's deconvolution algorithm (Lucy 1974) to the image and performed fits to the resulting surface brightness profiles. The difference between values of β and r_c for the original and the deconvolved images is insignificant. As the dispersion in r_c is small, the fits show that X-ray surface brightness can be reasonably approximated as being circularly symmetric, with errors due to deviations from circular symmetry being relatively small.

The above expression for the X-ray surface brightness profile can be readily inverted to yield the gas density profile

$$\rho(r) = \rho_0\left(1 + \frac{r^2}{r_c^2}\right)^{-3\beta/2} . \qquad (7.2)$$

The central density ρ_0 is proportional to the central electron density n_{e0}, which is given by

$$n_{e0} = \frac{1.2S_0(1+z)^4}{\Omega \Lambda r_c} \frac{\Gamma(3\beta)}{\Gamma(1/2)\Gamma(3\beta - 1/2)} , \qquad (7.3)$$

where S_0 is the central surface brightness, Ω is the solid angle of 1 arcmin^2 divided by 4π and Λ is the emissivity of the gas in the observed energy band. Formally, the above inversion assumes that the gas is isothermal and spherically distributed. However, for gas at temperatures of 2–15 keV, the photon count rate in the 0.5–2 keV PSPC energy band is relatively insensitive to temperature variations; for example, the values of n_{e0} computed assuming a gas temperature of $T = 3$ keV and $T = 8$ keV differ only by 5%–10%. The values of n_{e0} associated with the fits to the X-ray surface brightness profiles in each of the four quadrants are given in Table 1. At large radii, the gas surface density falls off as $\sim 1/r$, and since the X-ray surface brightness profile extends out to a projected distance of at least $\sim 9'$ ($\sim 1\ h^{-1}$ Mpc), so must the gas distribution.

Integrating the radial gas density distribution yields the total gas mass profile for the cluster. In Figure 18, we show the projected (two-dimensional) gas mass profile. The error bars reflect the uncertainties in the values of parameters (β, r_c) characterizing the surface brightness profile as well as in the value of the gas temperature at each radius. At the fiducial radius of 3'.5 ($\sim 400\ h^{-1}$ kpc), the projected gas mass is $(1.65 \pm 0.5) \times 10^{13}\ h^{-5/2}\ M_\odot$. Unlike the weak

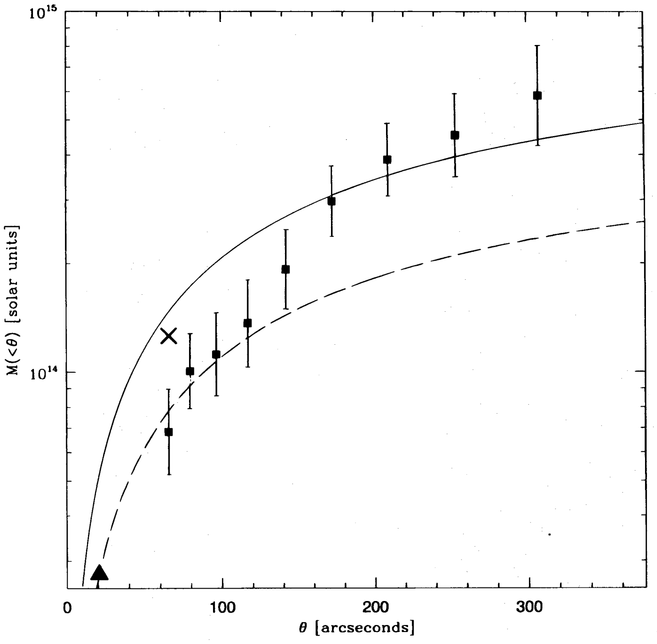

FIG. 16.—The two-dimensional mass profile of the cluster. The points with errors are the estimates from the weak lensing with the uncertainties calculated from adding the errors in κ and $\Sigma_{\rm crit}$ in quadrature. The mass calculation uses the surface density interior to a radius relative to that in the control region extending to $\theta = 370''$. The solid and dashed lines are isothermal sphere predictions for $\sigma = 1370$, 1000 km s^{-1}, respectively, assuming the cluster extends into the control annulus. The "X" represents the mass estimated by Kneib et al. (1995) by modeling the giant arcs. The triangle is the mass measured by Miralda-Escudé & Babul (1995) at the critical radius from the cD galaxy.

lensing mass estimate, the gas mass corresponds to the *actual* projected mass within a specified radius.

Under the assumption that the intracluster gas is in thermal pressure–supported hydrostatic equilibrium in the cluster potential, the X-ray data can also be used to estimate the total gravitational mass of the cluster:

$$M(<r) = -\frac{kT(r)r}{G\mu m_p}\left(\frac{d\ln\rho_g}{d\ln r} + \frac{d\ln T}{d\ln r}\right). \qquad (7.4)$$

TABLE 1

THE RESULTS OF THE ISOTHERMAL β FITS IN THE FOUR DIRECTIONS FROM THE HARD IMAGE DERIVED FROM THE PSPC DATA

Direction	r_c (kpc h^{-1})	β	n_{e0} (cm^{-3})
West	153	0.73	0.0068
	110	0.62	0.0076
South	144	0.78	0.0086
	110	0.67	0.0093
East	206	0.78	0.0064
	158	0.68	0.0069
North	138	0.75	0.0079
	86	0.63	0.0092

NOTE.—We used the PSPC data for fitting the models, as the statistics in that data set are much better than for the HRI data, owing to a lower background. The two different results for each direction correspond to 3 σ errors. Here n_{e0} is the central electron number density for 8 keV. The electron density is lowered by about 5%–10%, assuming a gas temperature of 3 keV.

This calculation, however, requires the knowledge of the temperature distribution in the cluster. The first *ASCA* observations give a temperature of $T = 8$ keV (Yamashita 1995), while *Ginga* observations yield an overall flux-weighted ICM temperature of $6.7^{+0.5}_{-0.4}$ keV (McHardy et al. 1990). A spectral analysis of the *ROSAT*/PSPC data, on the other hand, yields temperatures in the range of 3–5 keV. In this analysis, we fitted the temperature, the hydrogen column density, and the metallicity simultaneously in different annuli. The temperature determinations for the different radial bins agree within the error bars and are always lower than the *Ginga* or the *ASCA* determinations.

The discrepancy between our *ROSAT*-based determination of the gas temperature in A2218 and the temperature measurements from *ASCA* or *Ginga* may simply reflect the fact that the analysis of the *ROSAT* data do not provide results that are as accurate as the other two satellites in cases in which the peak of the ICM energy spectrum lies beyond the energy range of the PSPC. Alternatively, the discrepancy in the temperature determinations may indicate the presence of gas components with different temperatures, with the PSPC data being dominated by emission from the colder components while the *ASCA* and the *Ginga* data are dominated by the high-temperature component. Indeed, a new analysis of the *ASCA* data suggests that the gas temperature declines away from the cluster center (Mushotzky 1995). We did attempt a two-temperature fit to the X-ray spectra but did not find any improvement.

As noted above, our spectral analysis also yields a measure of the hydrogen column density and metallicity. We find a hydrogen column density in the range 1–3 × 10^{20} cm^{-2} and a metallicity of $0.2^{+0.2}_{-0.2}\,Z_\odot$. The metallicity agrees very well with the *Ginga* and the *ASCA* results of $0.2^{+0.2}_{-0.2}\,Z_\odot$ (McHardy et al. 1990) and 0.18 $Z_\odot$ (Yamashita 1995), respectively.

It should be noted that the results of the spectral analysis depend weakly on the adopted value for the background. In our analysis, we used values estimated from several different regions. In addition, the temperature and the hydrogen column density determinations also depend weakly on the data channels used. Ignoring the lower channels (channel 20–40; channels lower than 20 are always neglected because of the low efficiency of the *ROSAT*/PSPC in that energy range) increases the hydrogen column density and the temperature slightly.

In estimating the cluster mass from the X-ray data, we need to take into account the possibility of temperature gradients existing in the cluster as well as the uncertainty in the value of the overall ICM temperature. Indeed, a recent reanalysis of the *ASCA* data suggests that there is a significant temperature gradient, with the new estimate of the central temperature in good agreement with the *Ginga* result (Mushotsky 1995). As the mass estimates depend both on the radial temperature and its gradient (see eq. [7.4]), it is important to allow for variations away from isothermality. We accomplish this by using the Monte Carlo scheme of Neumann & Böhringer (1995) to determine the total mass profile. Briefly, we generate a temperature profile for the cluster by assigning a temperature, drawn randomly from a predefined range (3–8 keV in the present case), at equally spaced (60 h^{-1} kpc) locations along the radial direction. To prevent unrealistic short-scale oscillations in the temperature profile, we require the tem-

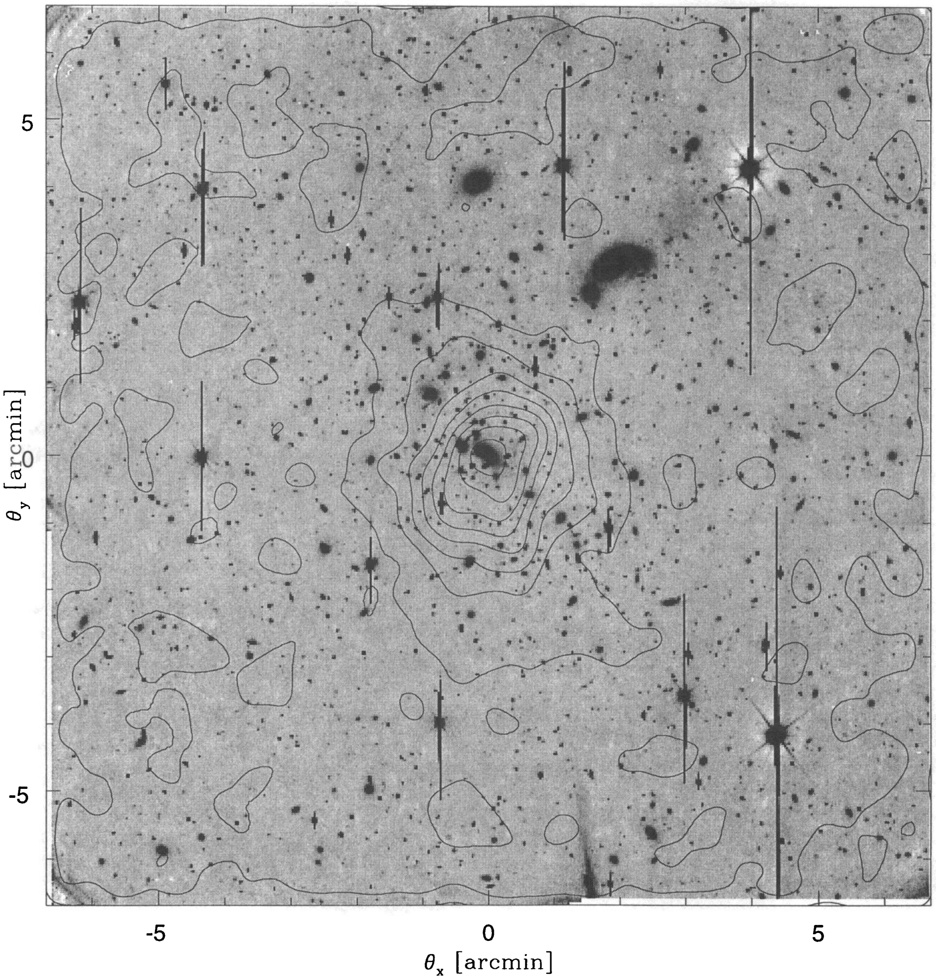

FIG. 17.—The HRI X-ray surface brightness profile placed on the optical image of the cluster. The contours have been smoothed with a Gaussian with scale length 0.'23. North is to the right; east is up.

peratures at adjacent locations to be within 0.6 keV of each other. At every step, we calculate the cumulative total mass profile and use only those temperature profiles that give a mass profile that increases monotonically with radius. To obtain an optimal estimate of the mean mass profile as well as the standard deviation, we generate 10^5 temperature profiles and compute the corresponding mass profiles. To ensure that our mass determination includes uncertainties in the gas density profile, we vary the values of (β, r_c) over the range given in Table 1 and repeat the above operations. The projected (two-dimensional) profile of the total mass derived from the X-ray data is shown in Figure 18. At the fiducial radius of 3.'5 ($\sim$400 h^{-1} kpc), the projected total mass is $(2.6 \pm 1.6) \times 10^{14}\ h^{-1}\ M_\odot$. As in the case of the gas mass estimates, the projected X-ray mass estimate, unlike the weak lensing estimate, corresponds to the *actual* projected mass within a specified radius.

Combining the above estimates of the gas mass and the total mass determined from the X-ray data yields a gas-to-total mass ratio of $M_{\rm gas}/M_{\rm tot} = (0.06 \pm 0.04)\ h^{-3/2}$. This is consistent with the value derived for the Virgo Cluster (Böhringer et al. 1994), and a typical value for clusters using the X-ray estimates for the gas and total mass is $M_{\rm gas}/M_{\rm tot} \sim 0.05\ h^{-3/2}$ (White & Fabian 1995; David et al. 1995).

8. DISCUSSION AND CONCLUSIONS

In this paper, we have reported on the detection of dark matter in the cluster of galaxies A2218. We found a strong, coherent shear pattern over a scale of $\sim$400″ from the cluster optical center. Using the weak lensing technique, we have mapped out the dark matter distribution. We have also analyzed the distribution of galaxies, of optical light, and of the X-ray emission associated with the cluster.

The combination of the optical, the lensing, and the X-ray data affords us an unprecedented opportunity to compare the relative distributions of the galaxies, the gas and the total mass in A2218. These distributions are displayed in Figures 7, 8, 15, and 17, respectively. In all the distributions, the location of the peak (or the dominant peak) corresponds to the location of the central cD galaxy/primary galaxy concentration. There are no strong distinct features associated with the secondary galaxy concentration. In the case of the light and the mass maps, it can be argued that the lack of such features may be a consequence of the poor resolution resulting from smoothing the maps on a scale of 0.'67. The X-ray map, however, is smoothed on the scale of 0.'23 and hence has a much higher resolution.

The contours immediately surrounding the central peak in both the light and the mass maps are elliptical, with the elongation extending in the direction of secondary galaxy clump. The X-ray contours in the immediate vicinity of the peak are also elliptical, but with the major axis oriented orthogonal to that of the mass and the light isocontours. The relative orientation of the isocontours in the mass and the X-ray maps is reminiscent of features seen in hydrody-

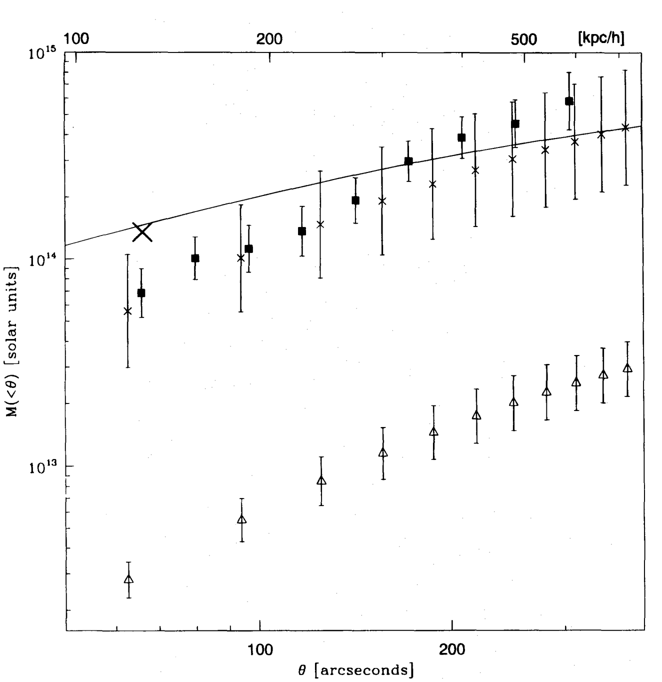

FIG. 18.—The two-dimensional mass profile of the cluster. The filled squares are estimates from the weak lensing. The crosses are total mass determined from the X-ray gas, with the error bars being the 2 σ dispersion calculated from the 10^5 simulations. The open triangles are the corresponding estimates of the projected gas mass. The solid line is the isothermal model with a velocity dispersion of 1370 km s^{-1}, and the large "X" represents the mass computed by Kneib et al. (1995) by modeling the giant arcs.

namical simulations of a cluster undergoing a merger with a subcluster (e.g., Schindler & Müller 1993). In such events, the X-ray emission tends to trace the lenticular shocks that expand in the direction perpendicular to the trajectory of the infalling subcluster. If this is indeed the case in A2218, then the gas in the central regions would not be expected to be in hydrostatic equilibrium, and this may help explain the discrepancy between lensing and the X-ray mass estimates reported by Miralda-Escudé and Babul (1995). However, smoothing the X-ray map on the same scale as the mass and the light maps yields an almost circular surface brightness profile and consequently, it is difficult to ascertain whether both the ellipticity and the orientation of the X-ray contours on scales smaller than ~1′ are significant.

At distances of 1′–3′ from the central peak, the extensions in the isodensity contours in the mass map closely follow those in the galaxy surface density plot and to a lesser degree, in the galaxy light distribution. The gas distribution as delineated by the X-ray surface brightness also appears to trace the mass closely. The X-ray map exhibits all the extensions in the mass map with the exception of one, the eastern extension.

At projected distances 3′ (~340 h^{-1} kpc) to 5′ (~600 h^{-1} kpc) from the cD galaxy, the radial surface density profiles of the cluster light, the intracluster gas, and the total mass are all consistent with a ~$1/r$ decrease. On these scales, there is no indication of the light or the gas distributions being biased with respect to the total mass.

The projected total mass within a fiducial radius of 3′.5 (~400 h^{-1} kpc) from the cD galaxy, as yielded by the weak lensing analysis, has a lower bound of $M_{\rm tot} = (3.9 \pm 0.7) \times 10^{14}\ h^{-1}\ M_\odot$. This value is in good agreement with the projected total cluster mass inferred from the X-ray data under the assumption that the gas is in thermal pressure–supported hydrostatic equilibrium. Since the projected gas mass interior to ~400 h^{-1} kpc is $(1.65 \pm 0.5) \times 10^{13}\ h^{-5/2}\ M_\odot$, the resulting gas-to-total fraction is $M_{\rm gas}/M_{\rm tot} = (0.06 \pm 0.04)\ h^{-3/2}$ if one adopts the cluster mass estimated using the X-ray data and $M_{\rm gas}/M_{\rm tot} = (0.04 \pm 0.02)\ h^{-3/2}$ if one uses the mass estimate derived from the lensing estimate.

Estimating the total stellar mass using a mean mass-to-light ratio of $M/L = 8\ h$, we find that its contribution to the total baryonic mass is negligible in comparison to the mass in the intracluster gas. The above values of $M_{\rm gas}/M_{\rm tot}$ suggests that the baryonic fraction in A2218, within the central ~400 h^{-1}, is $f_b \approx (0.04 \pm 0.02)\ h^{-3/2}$. Comparing this value to the mean baryonic fraction of the universe expected from nucleosynthesis arguments (e.g., Walker et al. 1991) of $f_b \leq 0.015(\Omega h^2)^{-1}$ suggests that the value of the cosmological density parameter is $\Omega \simeq 0.3$.

Furthermore, adding the light in the field associated with *all* the galaxies gives a lower bound on the mass-to-light ratio in A2218. At the fiducial radius, we find that $(M/L_B) = (440 \pm 80)\ h(M_\odot/L_{\odot B})$. If we use only the red light associated with the bright galaxies in the cluster color sequence, we obtain $(M/L_B) = 570\ h(M_\odot/L_{\odot B})$. Here we have used the lensing mass estimate and have derived the M/L ratio using the total projected mass and luminosity. This ratio remains roughly constant for $r = 180''$ out to the edge of our survey, since both the projected light and the surface mass density radial profiles vary with radius in a similar fashion. Converting the above M/L into an estimate of the cosmological density parameter once again yields $\Omega \simeq 0.3$.

As we discussed previously, the mean surface mass density used to determine the weak lensing mass estimate is, however, calculated by subtracting the mean in the reference annulus extending from 3′.5 to 6′.2. Only if the cluster mass distribution drops off sharply beyond ~400 h^{-1} kpc does the quoted value of the mass represent the actual value of the projected mass internal to ~400 h^{-1} kpc. If, however, the cluster mass distribution extends beyond ~400 h^{-1} kpc (and hence, into the reference annulus), then the above value is an underestimate. There are indications that the latter is true; for example, the X-ray surface brightness profile extends smoothly out to ~1 h^{-1} Mpc, and the projected cluster mass continues to rise at least out to ~600 h^{-1} kpc. If this is indeed so, then the actual value of the projected mass interior to ~400 h^{-1} kpc could potentially be much higher. We must caution, however, that this is a highly model-dependent scenario: the isothermal model gives the actual mass being a factor ~1.6 higher than our quoted value, while a steeper, Hernquist-type profile gives only a factor of ≃1.2.

From our observations, we can estimate the factor by which the lensing underestimates the mass through the following exercise. We start with the null hypothesis that the lensing and X-ray mass estimates agree. Under this assumption, we calculate, from the observed X-ray inferred mass profile, the mean surface mass density in the control annulus and find $\bar\kappa_{\rm X}(3'.5 < \theta < 6'.2) = 0.02 \pm 0.04$. From the lensing analysis, $\zeta(3'.5) = (0.11 \pm 0.02)$, so we can revise the lensing estimate of the mean surface density interior to the fiducial radius by $\bar\kappa(<3'.5) = \zeta(3'.5) + \bar\kappa_{\rm X}(3'.5 < \theta < 6'.2)$. This yields a new estimate for the mass inferred from the lensing of $M_{\rm tot}(\theta < 3'.5) = (4.6 \pm 1.4) \times 10^{14}\ h^{-1}\ M_\odot$. The X-ray mass estimate is $M_{\rm X} = (2.6 \pm 1.6) \times 10^{14}\ h^{-1}\ M_\odot$, hence, within the measured uncertainties, this is consistent with the null hypothesis that the lensing and X-ray mass estimates are in agreement. It is tantalizing that at 3′.5 the ratio of the lensing inferred mass to the X-ray determination is $M_{\rm lens}/M_{\rm X} \simeq 2{:}1$, as was found by Miralda-Escudé & Babul (1995) in the cluster center. However, the rather large uncertainties in our mass determinations do not allow us to conclude that this is a significant discrepancy at this radius.

The above exercise suggests that the correction to the lensing mass estimate due to the material in the control annulus is small ($\simeq 20\%$).

Still, it is tempting to speculate on the consequences of the cluster following an isothermal (r^{-1}) surface mass density profile in the control annulus (which is consistent with the cluster light and gas distributions). In this scenario, we have the following consequences: First, the lensing mass and the X-ray mass estimates would be discrepant by a factor of ≥ 2, with the lensing mass estimate being higher. Second, the gas-to-total mass ratio would drop to $f_b = (0.02 \pm 0.01)h^{-3/2}$, a result that is consistent with the nucleosynthesis value in an $\Omega = 1$ universe. Third, the mass-to-light ratio would also increase to a value as large as $M/L \sim 900$, implying a high value of Ω.

We can, at this point, speculate at length on whether or not the X-ray and lensing mass estimates are indeed discrepant away from the cluster center, and on whether our analysis of A2218 supports the case for high or low Ω. All these issues, however, can be settled observationally by probing directly the weak lensing distortions out to even larger radii and establishing whether or not the mass distribution associated with A2218 drops off sharply beyond a projected distance of 500 h^{-1} kpc. This exciting prospect is now possible with the advent of large-format CCD arrays; for example, the MOCAM device at CFHT has a 14′ prime focus field. As it comes into its own, the weak lensing technique offers a unique opportunity to resolve many of the outstanding puzzles regarding the dark matter content and distribution in the universe.

It is a pleasure to acknowledge most valuable assistance from Richard Griffiths and the MDS team. We are grateful to Megan Donahue for enlightening discussions on the X-ray map of the cluster. We thank Roser Pello for use of the compiled redshifts measured for the cluster field. We gratefully acknowledge the redshift data and extrapolation to faint magnitudes by Simon Lilly, Caryl Gronwall, and David Koo.

REFERENCES

Abell, G. O., Corwin, H. G., & Olowin, R. P. 1989, ApJS, 70, 1
Babul, A., & Katz, N. 1993, ApJ, 406, 51
Birkinshaw, M., & Gull, S. F. 1984, MNRAS, 206, 359
Birkinshaw, M., Gull, S. F., & Northover, K. 1981, MNRAS, 197, 571
Birkinshaw, M., & Hughes, J. P. 1994, ApJ, 420, 33
Böhringer, H., Briel, U. G., Schwarz, R. A., Voges, W., Hartner, G., & Trümper, J. 1994, Nature, 368, 828
Bonnet, H., Fort, B., Kneib, J.-P., Mellier, Y., & Soucail, G. 1994, A&A, 280, L5
Bonnet, H., & Mellier, Y. 1995, A&A, in press
Bonnet, H., Mellier, Y., & Fort, B. 1994, ApJ, 427, L83
Boynton, P. E., Radford, S. J., Schommer, R. A., & Murray, S. S. 1982, ApJ, 257, 473
Broadhurst, T. J., Taylor, A. N., & Peacock, J. A. 1995, ApJ, 438, 49
Butcher, H., Wells, D. C., & Oemler, A. J. 1983, ApJS, 52, 183
Coleman, G. D., Wu, C. C., & Weedman, D. W. 1980, ApJ, 43, 393
David, L. P., Jones, C., & Forman, W. 1995, ApJ, 445, 578
David, L. P., Slyz, A., Jones, C., Forman, W., Vrtilek, S. D., & Arnaud, K. A. 1993, ApJ, 412, 479
Davis, L. 1990, private communication
Fort, B., & Mellier, Y. 1994, A&A Rev., 5, 239
Fabricant, D., & Gorenstein, P. 1983, ApJ, 267, 535
Fahlman, G., Kaiser, N., Squires, G., & Woods, D. 1994, ApJ, 437, 56
Fischer, P., & Tyson, J. 1995, in preparation
Gronwall, C., & Koo, D. 1994, ApJ, 440, 1
Jones, M., et al. 1993, Nature, 365, 320
Kaiser, N., Broadhurst, T., & Squires, G. 1995c, in preparation
Kaiser, N., & Squires, G. 1993. ApJ, 404, 441
———. 1995, in preparation
Kaiser, N., Squires, G., & Broadhurst, T. 1995b, ApJ, 449, 460
Kaiser, N., Squires, G., Fahlman, G., & Woods, D., 1995a, in Clusters of Galaxies, ed. F. Durret, A. Mazure, & J. T. T. Van (Gif-sur-Yvette Cedex: Editions Frontières), in press
Klein, U., Rephaeli, Y., Schlickeiser, R., & Wielebinski, R. 1991, A&A, 244, 43
Kneib, J. P., Mellier, Y., Pello, R., Miralda-Escudé, J., Le Borgne, J., Böhringer, H., & Picat, J.-P. 1995, A&A, submitted
Landolt, A. U. 1992, A&A, 104, 340
Lilly, S. J. 1993, ApJ, 411, 501
———. 1995, private communication
Le Borgne, J. F., Pello, R., & Sanahuja, B., 1992, A&AS, 95, 87
Loeb, A., & Mao, S. 1994, ApJ, 435, 109
Lucy, L. 1974, AJ, 79, 745
McHardy, I. M., Stewart, G. C., Edge, A. C., Cooke, B., & Yamashita, K. 1990, MNRAS, 242, 215
Mellier, Y., Fort, B., Bonnet, H., & Kneib, J.-P. 1994, in Cosmological Aspects of X-Ray Clusters of Galaxies, ed. W. Seitter et al. (Boston: Kluwer), 441, 219
Miralda-Escudé, J., & Babul, A. 1995, ApJ, in press
Mushotzky, R. 1995, in Proc. 107th Meeting of the APS, Clusters, Lensing, and the Future of the Universe, in press
Neumann, D. M., & Böhringer, H., 1995, A&A, in press
Odewahn, S. C., Bryja, C., & Humphreys, R. M. 1992, PASP, 104, 553
Partridge, R. B., Perley, R. A., Mandolezi, N., & Delphino, F. 1987, ApJ, 317, 112
Pello, R., Le Borgne, J. F., Sanahuja, B., Mathez, G., & Fort, B. 1992, A&A, 266, 6
Pello-Descayre, R., Soucail, G., Sanahuja, B., Mathez, G., & Ojereo, E. 1988, A&A, 190, L11
Perrenod, S. C., & Henry, J. P. 1981, ApJ, 247, L1
Stewart, G. C., et al. 1994, in preparation
Schindler, S., & Müller, E. 1993, A&A, 272, 137
Schneider, P., & Seitz, C. 1995, A&A, 294, 411
Seitz, C., & Schneider, P. 1995a, A&A, 297, 287
Seitz, S., & Schneider, S. 1995b, preprint
Smail, I., Ellis, R. S., & Fitchett, M. J. 1994, MNRAS, 270, 245
Smail, I., Ellis, R. S., Fitchett, M. J., & Edge, A. C. 1995, MNRAS, 273, 277
Stark, A. A., Gammie, C. F., Wilson, R. W., Bally, J., Linke, R. A., Heiles, C., & Hurwitz, M. 1992, ApJS, 79, 77
Stetson, P. B., & Harris, W. E. 1988, A&A, 96, 909
Tresse, L., Hammer, F., le Fevre, O., & Proust, D. 1993, A&A, 277, 53
Tyson, J., & Fischer, P. 1995, ApJ, 446, 55
Tyson, J., Valdes, F., & Wenk, R. 1990, ApJ, 349, L19
Walker, T. P., Steigman, G., Kang, H., Schramm, D. M., & Olive, K. A. 1991, ApJ, 376, 51
White, D. A., & Fabian, A. C. 1995, MNRAS, 273, 72
White, S. D. M. 1992, in Clusters and Superclusters of Galaxies, ed. A. C. Fabian (Dordrecht: Kluwer), 17
White, S. D. M., Navarro, J. F., Evrard, A. E., & Frenk, C. S. 1993, Nature, 366, 429
Woods, D., Fahlman, G. G., & Richer, H. 1995, ApJ, 454, 32
Yamashita, K. 1995, in Clusters of Galaxies, ed. F. Durret, A. Mazure, & J. T. T. Van (Gif-sur-Yvette Cedex: Editions Frontières), 153